Journal of the European Ceramic Society 37 (2017) 4547–4557

Contents lists available at www.sciencedirect.com

Journal of the European Ceramic Society

journal homepage: www.elsevier.com/locate/jeurceramsoc

Additive and pyrolysis atmosphere effects on polysiloxane-derived porous SiOC ceramics

Donald Erb, Kathy Lu*

Department of Materials Science and Engineering, Virginia Tech, Blacksburg, VA,24061 USA

ARTICLE INFO

Article history:
Received 30 April 2017
Received in revised form 21 June 2017
Accepted 22 June 2017
Available online 24 June 2017

Keywords:
Silicon oxycarbide
Polymer derived ceramic
Porosity
Pyrolysis

ABSTRACT

Porous silicon oxycarbide (SiOC) is emerging as a much superior ultrahigh surface area material that can be stable up to high temperatures with great tailorability through composition and additive modifications. In this study, bulk SiOCs were fabricated from a base polysiloxane (PSO) system by using different organic additives and pyrolysis atmospheres followed by hydrofluoric acid (HF) etching. The additives modify the microstructural evolution by influencing the SiO_2 nanodomain formation. The SiOC ceramics contain significantly less SiC and more SiO_2 with $Ar+H_2O$ atmosphere pyrolysis compared to Ar atmosphere pyrolysis. Water vapor injection during pyrolysis also causes a drastic increase in specific surface areas. The addition of 10 wt% tetraethyl orthosilicate (TEOS) with $Ar+H_2O$ pyrolysis produces a specific surface area of 1953.94 m^2/g, compared to 880.09 m^2/g for the base PSO pyrolyzed in Ar. The fundamental processes for the composition and phase evolutions are discussed as a novel pathway to creating ultrahigh surface area materials. The ability to drastically increase the specific surface area through the use of pyrolysis atmosphere and organic additives presents a promising processing route for highly porous SiOC ceramics.

1. Introduction

Polymer derived ceramics are a family of materials with widely tailorable properties and compositions, including SiOC, SiCN, and SiBCN, for which polymer precursors undergo thermal decomposition and bond breaking/rearrangement, resulting in amorphous or nanocrystalline ceramics, depending on the pyrolysis temperature, with a wide range of never-before properties, such as high temperature stability, oxidation resistance, and electrical conductivity [1–3]. One such system is porous SiOC, which can be used as catalyst supports, thermal barriers, gas separation membranes, and lightweight components [4]. SiOC can be fabricated with a wide range of porosity from macropores to micropores using several different processing routes such as sacrificial templating, sacrificial filler [5], direct foaming, polymer precursor phase separation [6,7], and removal of certain phases after pyrolysis [8]. Out of all these methods, only phase separation and/or phase removal after pyrolysis can create uniformly distributed pores with single nanometer sizes (diameter <10 nm).

In detail, single nanometer pores resulting from phase separation can be introduced using two different methods. The first is through phase separation of the polymer precursors during crosslinking. Using immiscible polymers as precursors, it is possible to have two distinct phases after crosslinking. One of the phases then decomposes during pyrolysis, leaving behind pores. The resulting ceramics have high specific surface areas at temperatures around 600 °C [6]. However, depending on the specific precursors, the specific surface area may decrease as the temperature increases above 600 °C, due to the sintering of transient pores [6,9]. The second method is by controlling the phase separation and/or crystallization during pyrolysis. At temperatures above 1100 °C, the amorphous SiOC ceramic phase separates into free carbon and amorphous SiO_2 nanodomains. Annealing at higher temperatures results in further growth of the SiO_2 phase, as well as nanocrystalline SiC formation [10,11]. If these ceramic phases can be controlled to have homogenous nucleation and growth, high concentration, and single nanometer size, they can be etched away using hydrofluoric acid (HF) or chlorine gas, respectively, leaving behind single nanometer pores [1,12].

Controlling the chemistry of the polymer precursors can have drastic effects on the extent of phase separation during the crosslinking and pyrolysis of the SiOC. In previous studies with C-rich precursors, the resulting ceramic does not experience extensive phase separation even at high temperatures; instead the

* Corresponding author at: 213 Holden Hall, Virginia Tech, Blacksburg, VA 24061, USA.
E-mail address: klu@vt.edu (K. Lu).

http://dx.doi.org/10.1016/j.jeurceramsoc.2017.06.036
0955-2219/

system remains mostly amorphous SiOC and free carbon [2,13]. Alternatively, Si-rich precursors result in little to no free carbon and extensive crystallization of SiC and Si phases [10]. Turquat et al. [14] varied the Si, O, and C compositions of the polymer precursors through the use of triethoxysilane (TREOS) and dimethyldiethoxysilane (MDES). When the TREOS/MDES ratio is 1, giving a carbon rich polymer precursor, the resulting ceramic after pyrolysis and annealing at 1400 °C contains only a small volume fraction of SiC; free carbon is dispersed within the amorphous SiOC. When the TREOS/MDES ratio is 9, representing a Si rich polymer, the ceramic after 1400 °C annealing shows more SiC and Si nanocrystallites ranging from 20 nm to 50 nm in size. Thus, the size and amount of the nanodomains, and ultimately the pores after etching, can be controlled by varying the compositions of the precursors.

The second method to control the phases formed during pyrolysis is by introducing reactive species into the pyrolysis atmosphere, such as H_2 or H_2O [15–18]. Previous work in our lab demonstrated that injecting water vapor during the temperature range at which precursor bond (chain) breaking occurs results in a dramatic decrease in carbon precipitation and an increase in Si—O—Si bond formation [8,17,18]. The resulting SiOC sample pyrolyzed at 1300 °C after HF etching has a specific surface area of 2391.6 m^2/g, much greater than the specific surface area of the sample pyrolyzed in Ar at the same temperature, which was 630.41 m^2/g. Liang et al. [15] investigated water vapor injection effects on the chemistry and atomic bonding of SiOC from 500 °C to 1000 °C. The samples pyrolyzed in the water vapor atmosphere have only about half of the carbon content compared to the samples pyrolyzed in Ar, resulting in a reduction of SiC_4 and SiC_2O_2 structural units and an increase in SiO_4 units.

In this work, micro- and *meso*-porous SiOC ceramics are fabricated using different additives and pyrolysis atmospheres from polysiloxane (PSO)-based precursors. After pyrolysis, the ceramics are etched with a HF solution to create single nanometer pores. The effects of the additives and pyrolysis atmospheres on the resulting thermophysical properties, phase evolution, specific surface area, and pores of the SiOC ceramic are studied. The fundamental microstructural evolution mechanisms are proposed.

2. Experimental procedures

A commercial polysiloxane (PSO, $[-Si(C_6H_5)_2O-]_3[-Si(CH_3)(H)O-]_2[-Si(CH_3)(CH=CH_2)O-]_2$, viscosity ~ 2–10 Pa·s, SPR-684, Starfire Systems, Inc., Schenectady, NY) with alkyl, aryl, hydrogen, and vinyl side groups was chosen as the base of the precursor and 2.1–2.4% platinum-divinyltetramethyldisiloxane complex in xylene (Pt catalyst, Gelest Inc., Morrisville, PA) was used as the catalyst. The chemicals used as additives were polymethylphenylsiloxane (PMPS, $[-Si(CH_3)(C_6H_5)O-]_n$, viscosity ~ 0.45–0.55 Pa·s, Sigma-Aldrich, St. Louis, MO), polydimethylsiloxane (PDMS, $[-Si(CH_3)_2O-]_n$, Sylgard 184 10:1 base to curing agent, MW ~ 60000 g/mol [19], Dow Corning, Auburn, MI), polyhydromethylsiloxane (PHMS, $[-Si(CH_3)(H)O-]_n$, MW ~ 1400–1800 g/mol, Gelest Inc., Morrisville, PA), tetraethyl orthosilicate (TEOS, $Si(OC_2H_5)_4$, Sigma-Aldrich, St. Louis, MO), and tetramethyl orthosilicate (TMOS, $Si(OCH_3)_4$, Sigma-Aldrich, St. Louis, MO).

First, PSO and one of the five additives were mixed in a 9:1 weight ratio and magnetically stirred at approximately 350 rpm for 20 min to form a homogeneous mixture. Next, the Pt catalyst (1 wt% relative to PSO) was added, the mixture was magnetically stirred again at 350 rpm for 5 min, and then poured into an aluminum foil mold. In order to reduce cracking caused by the bubbles from the mixing of the precursors, the mixture was placed into a vacuum chamber and vacuumed for 30 min to approximately 1500 mTorr. After that, the mixture was put in an oven to crosslink at 50 °C for 12 h and then at 120 °C for 6 h. The samples with either TMOS or TEOS additives initially had slightly greater than 10 wt% of the additive added in order to account for the evaporation of the additives in the vacuum chamber. The TMOS and TEOS samples were also sealed during the curing process to prevent further evaporation. The samples designated as 100PSO corresponded to the pure PSO sample; the samples with additives were labelled as 10X, where X was either PMPS, PDMS, PHMS, TEOS, or TMOS.

To prepare the samples for pyrolysis, the crosslinked polymers were first cut and polished into circular pieces roughly 10 mm in diameter and 2 mm in thickness. Next, the samples were placed into a zirconia crucible, covered on both sides with graphite mats in order to reduce friction during shrinkage and prevent warping [20,21], and put into a tube furnace (1730-20 Horizontal Tube Furnace, CM Furnaces Inc., Bloomfield, NJ). The samples were heated up to 1400 °C at a rate of 1 °C/min, held for 2 h, cooled to 400 °C with a rate of 1 °C/min, and finally cooled to 50 °C with a rate of 2 °C/min. The Ar gas flow rate was held constant at about 500 std cm^3/min; for the samples with water vapor atmosphere, the Ar gas was bubbled through water at 60 °C when the furnace was at 500 °C–700 °C, giving a gas flow with a Ar:H_2O molar ratio of approximately 5:1. The 500 °C–700 °C water vapor injection temperature range was chosen because it corresponded to the temperature range at the majority of the decomposition occurs for both the base material [21] and the additives [6,22], allowing the water vapor to penetrate the entire sample due to micropores created by the decomposition [15].

Etching of the bulk SiOC samples after pyrolysis was done using a solution of HF (20 wt% HF in water). The HF solution was magnetically stirred at room temperature until the SiOC samples had no significant mass loss, taking approximately 4 days. The SiOC samples were then rinsed with deionized water and dried at 120 °C. The mass loss due to etching was calculated by dividing the change in mass after etching by the original mass.

Volumetric shrinkage and ceramic yield were calculated by measuring the dimensions and mass, respectively, of the samples before and after the pyrolysis; density was calculated by dividing the mass after pyrolysis with the measured volume and through the use of Archimedes method with ethanol as the medium. The phase compositions of the pyrolyzed samples were analyzed in an X'Pert PRO diffractometer (PANalytical B.V., EA Almelo, the Netherlands) with Cu Kα radiation. The JCPDS reference cards used to identify the crystalline phases were 00-039-1425 for SiO_2, 00-029-1129 for SiC, and 01-075-1621 for C. The chemical bonding was evaluated using Fourier Transform Infrared Spectroscopy (FT-IR) (Nicolet 8700 with Pike GladiATR attachment, Thermo Scientific, Waltham, MA), which recorded between 500 and 4000 cm^{-1} wavenumber with a resolution of 4 cm^{-1} and averaged between 64 scans; the powder samples for the FT-IR were prepared by grinding the bulk samples with a mortar and pestle. The specific surface area, pore size distribution, and pore volume of the pyrolyzed samples were evaluated using nitrogen adsorption at 77 K with a Quantachrome Autosorb-1 (Quantachrome Instruments, Boynton Beach, FL), and the samples were degassed before testing for 3 h at 300 °C. The pore size distribution and pore volume were derived by applying the Non Local Density Functional Theory (NLDFT) to the adsorption branch of the data [23]. The partial pressure range used to calculate the BET specific surface area was selected following the guidelines established by Rouquerol et al. [24] Assuming cylindrical pores, the average pore size was estimated using 4000 V/A, where V is the pore volume and A is the specific surface area [25]. The TEM sample was prepared by grinding the etched sample in a mortar and then dispersing in absolute ethanol; the microstructure was examined by a field emission analytical transmission electron microscope (JEOL 2100, JEOL USA, Peabody, MA).

Table 1
Volume shrinkage, ceramic yield, and density of the SiOC samples after 1400 °C pyrolysis.

Sample	Volumetric Shrinkage (%)		Ceramic Yield (%)		Density (g/cm^3) ± 0.02[a]	
	Ar	Ar + H_2O	Ar	Ar + H_2O	Ar	Ar + H_2O
100PSO	53.33 ± 1.15	53.07 ± 1.16	67.08 ± 0.71	66.71 ± 1.04	1.87	1.80
10PMPS	56.09 ± 0.62	49.33 ± 1.44	63.01 ± 1.06	66.62 ± 1.32	1.85	1.75
10PDMS	56.50 ± 1.74	52.46 ± 1.49	65.38 ± 1.97	68.39 ± 1.49	1.87	1.78
10PHMS	50.19 ± 0.64	50.63 ± 0.82	69.40 ± 2.15	71.93 ± 1.52	1.89	1.82
10TEOS	56.70 ± 1.48	50.30 ± 1.03	61.16 ± 0.30	66.50 ± 0.84	1.89	1.80
10TMOS	52.25 ± 3.34	50.43 ± 1.05	68.14 ± 4.78	71.30 ± 1.41	1.81	1.82

[a] Estimated error using Archimedes method.

3. Results and discussion

3.1. Thermophysical properties

The volume shrinkage, ceramic yield, and density values for the samples after pyrolysis are shown in Table 1. For the samples pyrolyzed in Ar, the volume shrinkage ranges from 50.19% to 56.70%, the ceramic yield ranges from 61.16% to 69.40%, and the density ranges from 1.81 g/cm^3 to 1.89 g/cm^3. Likewise, the samples pyrolyzed with water vapor have shrinkage values from 49.33% to 53.07%, ceramic yield values between 66.50%–71.93%, and densities in the range of 1.75 g/cm^3–1.82 g/cm^3.

The shrinkage and mass loss of the samples during pyrolysis are due to the release of hydrocarbons and hydrogen present in the preceramic [21]. During the pyrolysis in the Ar atmosphere, polymer preceramics containing higher amounts of hydrocarbons should experience greater shrinkage and lower ceramic yield. The volumetric shrinkage and ceramic yield values in Table 1 agree with this general trend. The preceramic containing the additive with the lowest hydrocarbon mass, PHMS, has the least shrinkage (50.19%) and the highest yield (69.40%), while the preceramic containing the additive with the highest hydrocarbon concentration, TEOS, shows the highest shrinkage (56.70%) and the lowest yield (61.16%). Further, the higher yield and low shrinkage for the 10PHMS sample may also arise due to reactions between the excess hydrogen bonds and either residual vinyl bonds or methyl bonds that occur between 500 and 700 °C, forming additional Si—CH_2—Si bonds and strengthening the polymer network [26]. The volumetric shrinkage, ceramic yield, and densities for the samples are comparable to those SiOCs derived from carbon rich precursors, and the densities are lower than other carbon poor SiOC systems due to a high amount of turbostratic carbon (density = 1.45 g/cm^3) [17,18,21].

Compared to the Ar pyrolysis, the SiOC samples pyrolyzed with water vapor injection generally show less volume shrinkage, higher ceramic yield, and lower density. The decrease in shrinkage and density for the Ar + H_2O samples is due to more extensive formation of the less dense SiO_2 (density = 2.2 g/cm^3) phase rather than SiC (density = 3.2 g/cm^3). The increase in ceramic yield for the Ar + H_2O pyrolysis is due to the incorporation of more oxygen within the SiOC in place of carbon, as to be discussed in Section 3.2.

3.2. Phase evolution

To understand the effect of the additives on the bonding differences after crosslinking, the FT-IR spectra of the crosslinked polymers are shown in Fig. 1. All samples show sharp peaks at approximately 695, 715, and 740 cm^{-1}, which are characteristic of silicon bonded with two phenyl side groups, found only in the base PSO, as well as a broad peak between 1000 and 1100 cm^{-1} assigned to Si—O—Si [27]. As to be explained later in Section 3.2, the main bonds that contribute to the reactions with water vapor are Si—H, Si—CH_3, Si—C_6H_5, Si—CH=CH_2, which are found within the base PSO and/or the additives, as well as Si—CH_2—CH_2—Si due to the hydrosilylation reaction between hydrogen and vinyl groups [28], and Si—CH_2—Si due to reactions between hydrogen, methyl, and Si—CH_2—CH_2—Si groups occurring at 500 °C–700 °C [26,29].

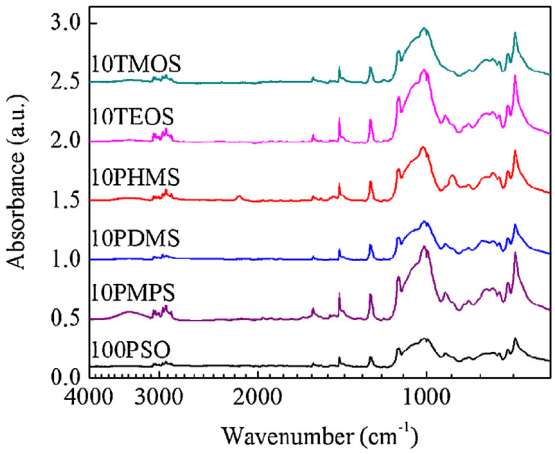

Fig. 1. FT-IR spectra for the polymer precursors after crosslinking.

The base PSO polymer contains equal molar amounts of hydrogen and vinyl groups, so the Si—H and Si—CH=CH_2 groups should be consumed during crosslinking [28]. Indeed, none of the polymers show the characteristic Si—H peak at 2160 cm^{-1} except for 10PHMS, due to the additional hydrogen bonds in the PHMS additive. The vinyl side group, which shows peaks at 1600 cm^{-1}, 3050 cm^{-1}, and 3070 cm^{-1} [18], is hard to distinguish for these polymers due to their overlap with the peaks of the phenyl side group; however, due to the lack of the Si—H peaks for all the samples except for the 10PHMS, it can be assumed that the majority of vinyl groups have been likewise consumed during crosslinking. Thus, the major bonds present in the samples that will react with water vapor during pyrolysis are Si—CH_3, Si—C_6H_5, Si—CH_2—CH_2—Si, and Si—CH_2—Si, as well as Si—H for the 10 PHMS sample. The main bonds found in the FT—IR spectra for the polymers are summarized in Table 2.

Table 2
Major FT-IR peaks identified in the crosslinked polymers [27,30].

Wavenumber (cm^{-1})	Functional Group
693	Si-phenyl
715	Si-phenyl
739	Si-phenyl
950–1100	Si—O—Si
1130	Si—phenyl
1259	Si—CH_3
1426	Si-phenyl
1590	C=C in phenyl
2150	Si—H
2890–2976	C—H_x
3000–3100	C—H in phenyl
3100–3700	—OH

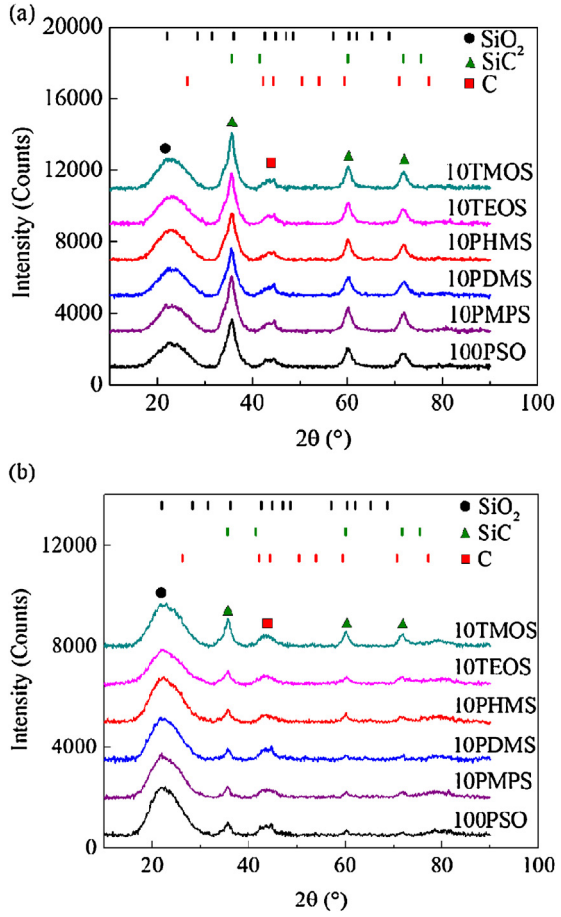

Fig. 2. XRD patterns for different polymer precursors after 1400 °C pyrolysis in (a) Ar and (b) Ar + H_2O.

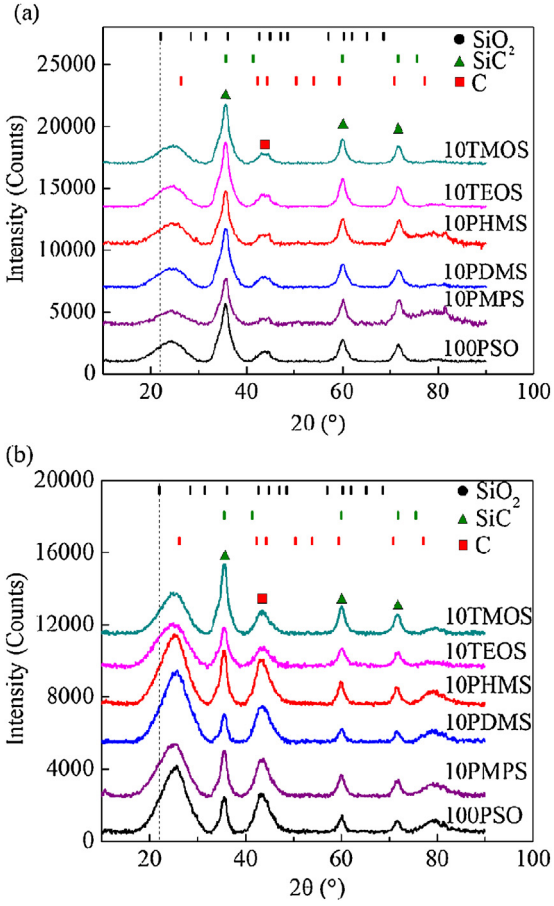

Fig. 3. XRD patterns after the HF etching of the SiOC samples pyrolyzed in (a) Ar and (b) Ar + H_2O.

Fig. 2(a) shows the XRD patterns for the SiOC samples pyrolyzed in Ar at 1400 °C. All the samples show an amorphous SiO_2 halo centered around ~23° and SiC peaks at 35.6°, 60°, and 72° [25]. In addition, all the samples exhibit a peak at ~44°, which corresponds to the (100) plane of turbostratic carbon [25,31–33]. The presence of the SiO_2, SiC, and carbon diffraction peaks for the samples after pyrolysis occurs due to the phase separation of SiOC, as well as the carbothermal reduction of SiO_2 into SiC. The main reactions that produce SiO_2, SiC, and C within the ceramics are given by the following reactions [11,34]:

$$2SiOC \rightarrow SiO_2(amorphous) + SiC(\beta) + C \quad (1)$$

$$SiO_2(amorphous) + 3C \rightarrow SiC(\beta) + 2CO\uparrow \quad (2)$$

Comparison of the intensity of the SiO_2 halo to that of the SiC peak at 35.6° for each sample shows that the 10PMPS sample has the highest SiC to SiO_2 ratio with a value of 2.0, while the 10PHMS sample has the lowest with a ratio of 1.5; this result is due to the higher concentration of carbon for the 10PMPS sample, which leads to more carbothermal reduction of SiO_2.

Fig. 2(b) shows the XRD patterns for the SiOC samples pyrolyzed in Ar + H_2O at 1400 °C. All samples show reduced SiC peaks at 35.6°, 60°, and 72° compared to the samples pyrolyzed in Ar due to the decrease of Si-C bonds in the water vapor environment [15]. With the presence of water vapor between 500 °C and 700 °C, the polymer to ceramic transformation occurs with the following additional possible reactions [15,17]:

$$Si{-}H + H_2O \rightarrow Si{-}OH + H_2\uparrow \quad (3)$$

$$Si{-}CH_3 + H_2O \rightarrow Si{-}OH + CH_4\uparrow \quad (4)$$

$$Si{-}CH_2{-}Si + H_2O \rightarrow Si{-}OH + Si{-}CH_3 \quad (5)$$

$$Si{-}CH_2{-}CH_2{-}Si + 2H_2O \rightarrow 2Si{-}OH + C_2H_6\uparrow \quad (6)$$

$$Si{-}CH{=}CH_2 + H_2O \rightarrow Si{-}OH + C_2H_4\uparrow \quad (7)$$

$$Si{-}C_6H_5 + H_2O \rightarrow Si{-}OH + C_6H_6\uparrow \quad (8)$$

The Si—OH bonds further condense to form Si—O—Si bonds:

$$Si{-}OH + Si{-}OH \rightarrow Si{-}O{-}Si + H_2O\uparrow \quad (9)$$

In addition, free carbon that precipitates between 500 °C and 700 °C also oxidizes following the reaction [15,18,35]:

$$C_{free} + H_2O \rightarrow H_2\uparrow + CO\uparrow \quad (10)$$

According to Eqs. (3)–(10), water vapor facilitates Si—O bond formation while reducing Si—C bonds and consuming free carbon; the diffraction patterns in Fig. 2(b) for all of the samples clearly reflect this.

The XRD patterns for the SiOC samples pyrolyzed at 1400 °C in Ar and Ar + H_2O after the HF etching are shown in Fig. 3(a) and (b), respectively. Dotted lines show the original position of the amorphous hump before etching. The samples no longer show the amorphous SiO_2 hump around 23°; rather, the center of the diffused peak shifts to approximately 24.5°, due to the contributions of both the remaining SiOC and the turbostratic carbon which has a peak at 26° from the (002) plane [32,33,36]. The etching of the SiO_2 nanodomains by the HF solution follows the reaction [18]:

$$SiO_2 + 6HF \rightarrow H_2SiF_6 + 2H_2O \quad (11)$$

Thus, the shift of the 23° hump in Fig. 3(a) and (b) signifies that the SiO_2 nanodomains are removed by HF, while the remain-

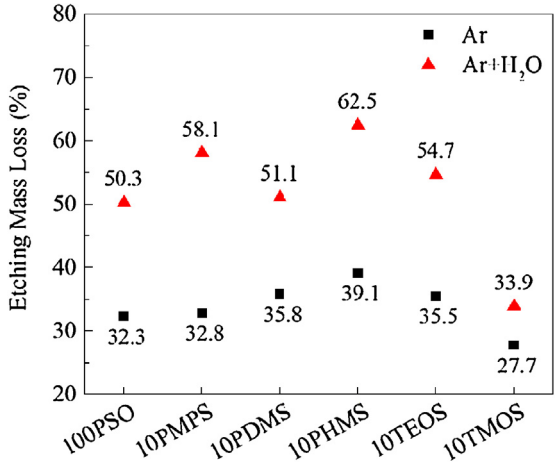

Fig. 4. Mass loss after the HF etching for both the Ar and Ar + H_2O pyrolysis conditions.

ing SiOC, SiC, and C are largely unaffected [37]. In addition, a new diffraction peak emerges after etching at approximately 78°, which corresponds to the (110) plane of carbon [33]. The increase in the intensity of the SiC and C peaks after the HF etching, especially for the Ar + H_2O samples, is due to the removal of SiO_2 from the sample, which effectively increases the concentration of the remaining phases.

The amount of mass loss due to the HF etching for the samples pyrolyzed in Ar and Ar + H_2O are shown in Fig. 4. For the samples pyrolyzed in Ar, the mass loss from the HF etching ranges from 27.7 to 39.1%. For the samples with water vapor injection, the mass loss after etching increases for all the samples and ranges from 33.9 to 62.5%. The increase in the mass loss with the water vapor atmosphere can be attributed to SiO_2 enrichment due to Si—C bonds being converted to Si—O bonds, as discussed previously. The impact is significant, up to 77% increase in the mass loss. Interestingly, the 10TMOS sample shows similar mass losses for both the Ar and Ar + H_2O atmospheres. This means that the TMOS additive does not contribute significantly to the SiO_2 formation. It is likely that the molecular mixing with the PSO precursor leads to more SiOC formation than SiO_2 formation, which is also supported by the nitrogen adsorption data in Section 3.3.

The FT-IR patterns for two of the SiOC samples, 100PSO and 10TMOS, after pyrolysis at 1400 °C in Ar and Ar + H_2O, are shown in Fig. 5(a) and (b), respectively. No other samples were tested due to their similar phase behaviors with the 100PSO sample in both of the atmospheres as already seen with the XRD results in Fig. 2 and Fig. 3. Both the 100PSO and 10TMOS samples pyrolyzed in Ar show peaks around 1050 cm^{-1} and 800 cm^{-1}, corresponding to Si—O—Si and Si—C bonds, respectively [38]. The relative intensities of the peaks show no major difference between the two precursors; the 1050 cm^{-1}:800 cm^{-1} peak intensity ratio for 100PSO and 10TMOS is 1.8 and 2.1, respectively. For the pure PSO sample pyrolyzed in Ar + H_2O, there is a drastic increase in the height of the Si—O—Si peak relative to the Si—C peak compared to the sample pyrolyzed in Ar. The 10TMOS sample, however, does not show such a drastic difference between the Ar and Ar + H_2O conditions, as also seen in Fig. 2(b), due to a lesser extent of reaction between H_2O and the polymer. For the Ar + H_2O pyrolyzed samples, the 1050 cm^{-1}:800 cm^{-1} peak intensity ratios for 100PSO and 10TMOS are 4.2 and 3.1, respectively. After etching with HF, both samples show a drastic decrease in the Si—O—Si peak due to the HF removal of SiO_2 as explained earlier. As a matter of fact, the Si—O—Si peak for all the HF etched samples almost disappears.

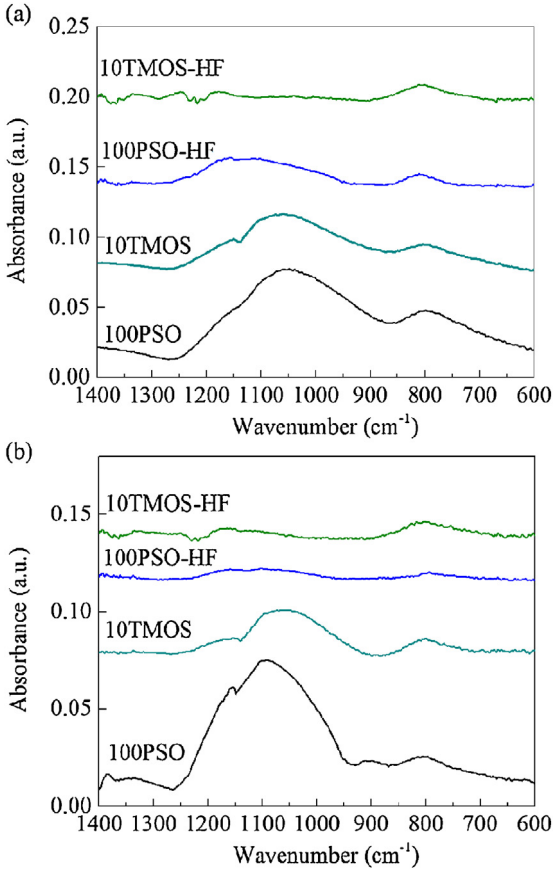

Fig. 5. FT-IR patterns for the SiOC samples with different additives pyrolyzed in (a) Ar and (b) Ar + H_2O before and after the HF etching.

3.3. Specific surface areas and pores

Fig. 6(a) and (b) show the nitrogen adsorption curves for the samples pyrolyzed in Ar and Ar + H_2O, respectively. All the samples pyrolyzed in Ar show a large adsorption volume at low relative pressures, followed by a relatively constant adsorption volume at higher relative pressures; this adsorption behavior corresponds to the Type I isotherm, according to the IUPAC classification, which indicates that the samples are prominently microporous with only monolayer adsorption [39]. The 10TMOS sample also displays more adsorption at higher relative pressures, indicative of a broader pore size distribution. In general, the adsorbed volume is from 252.8 cm^3/g to 311.4 cm^3/g at $P/P_o = 1$.

For the samples pyrolyzed in Ar + H_2O, the 100PSO, 10PHMS, and 10PMPS samples display similarly large adsorption volumes at low relative pressures, followed by a further increase in adsorption at higher relative pressures due to multilayer gas adsorption. These adsorption characteristics correspond closer to the Type IV isotherm, indicative of materials containing both micropores and mesopores [39]. The 10TMOS, 10TEOS, and 10PDMS samples still display the Type I isotherm adsorption behavior after the Ar + H_2O atmosphere pyrolysis. This means that the Ar + H_2O atmosphere creates significant mesopores for the more C-rich additive systems but not for the more O-rich additives. As a result, the adsorption volume is from 324.3 cm^3/g to 662.3 cm^3/g at $P/P_o = 1$, varying greatly compared to that of the Ar atmosphere pyrolyzed samples. In general, the adsorption volumes are much higher (100PSO, 10PMPS, and 10PHMS samples are more than 100% higher) than those of the samples pyrolyzed in the Ar atmosphere. Alternatively, the 10TEOS sample for the Ar + H_2O condition shows a much greater adsorption volume at low relative pressures due to a large number of micro-

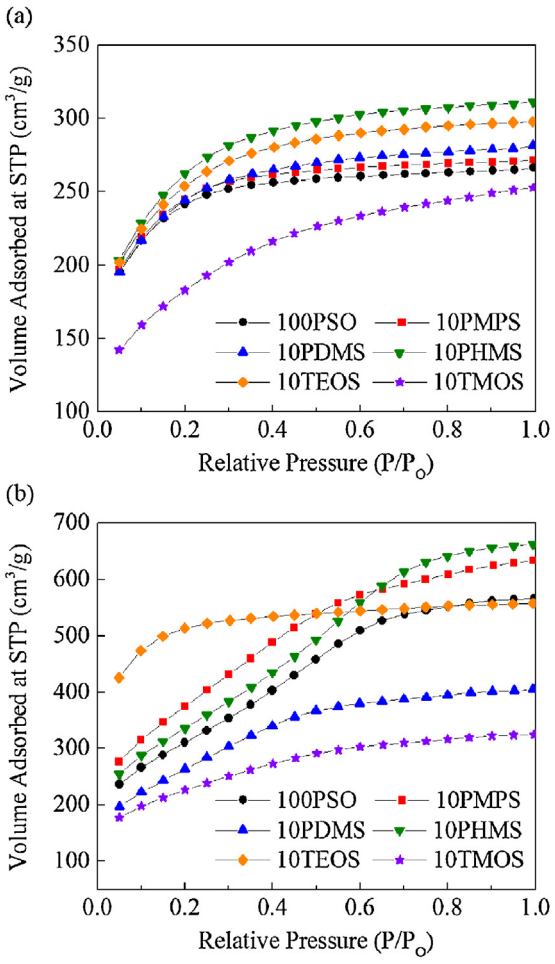

Fig. 6. Nitrogen adsorption curves for the samples pyrolyzed at 1400 °C in (a) Ar and (b) Ar + H_2O.

pores and the volume adsorbed does not increase significantly as the relative pressure increases, indicating that mesopores are not widely present in the sample.

The specific surface area, average pore size, micropore volume, and total pore volume for all of the samples in the Ar and the Ar + H_2O pyrolysis atmospheres are summarized in Table 3.

For the samples pyrolyzed in Ar, the specific surface area ranges from 653.41 to 952.64 m^2/g. The addition of PMPS and PDMS has little effect on the specific surface area of the base PSO, and the addition of TEOS and PHMS increases the specific surface area slightly by 40–70 m^2/g; TMOS greatly reduces the specific surface area by ~300 m^2/g from 952.64 m^2/g to 653.41 m^2/g. Pyrolysis with water vapor, however, drastically increases the specific surface area for all the samples, with the specific surface areas ranging from 804.24 m^2/g to 1953.94 m^2/g. This means that water vapor pyrolysis can significantly facilitate the SiO_2 cluster formation during the pyrolysis and thus the resulting porous SiOC specific surface area, as to be discussed in Section 3.4.

After pyrolysis in Ar, the average pore sizes range from 1.77 to 2.27 nm. In general, the average pore size increases as the carbon content of the polymer precursor decreases (100PSO → 10PMPS → 10PDMS → 10PHMS → 10TEOS → 10TMOS). This is because the graphitic carbon domains that separate the SiO_2 clusters act as diffusion barriers for SiO_2 and prevent further growth of the SiO_2 clusters [34]. Thus, for the samples with lower carbon content, the size of the pores created by etching the SiO_2 clusters would be larger since the diffusion and growth of SiO_2 are greater relative to those of the samples with higher carbon content. For the Ar + H_2O atmosphere pyrolysis, all the samples except for 10TEOS experience an increase in average pore size, ranging from 1.66 to 3.27 nm. Also, the average pore size for the samples generally decreases as the precursor carbon content decreases, with the exception of the 10PHMS sample; the 10TMOS sample has similar average pore sizes for both pyrolysis conditions, and the 10TEOS sample actually experiences a decrease in the average pore size after the Ar + H_2O pyrolysis. The reason for this phenomenon can be understood as follows. During the Ar + H_2O atmosphere pyrolysis, TEOS has a high amount of Si—O bonds available to form new SiO_2 clusters independently. These SiO_2 clusters are small yet numerous in number. After the HF etching, the average pore size from the SiOC matrix-induced SiO_2 nanoclusters and the TEOS-induced SiO_2 nanoclusters is smaller than the SiO_2 size from the SiOC matrix only. This compounding effect is also reflected from the pore volume results. The pore volume for the Ar + H_2O pyrolyzed sample is higher than that for the Ar atmosphere pyrolyzed sample; it is also much higher than the pore volume with the TMOS additive. Based on these results, it can be stated that for an additive to increase the specific surface area, separate SiO_2 nucleation must be activated yet controlled so that the new SiO_2 final size is no larger than the SiOC phase separation induced SiO_2 size. Any additive that simply facilitates the SiOC matrix-based SiO_2 formation and growth is not desired. This is conjectured to be what happens to the TMOS additive, which likely has an intimate mix with the PSO matrix. TMOS may hydrolyze (as described in Eq. (12)) yet cannot lead to independent SiO_2 nucleation. Subsequently, it leads to more advanced SiOC matrix-induced SiO_2 nucleation and growth. As a result, the SiO_2 nanodomain size is larger than that without TMOS, and the specific surface areas for both the Ar and Ar + H_2O atmosphere pyrolysis conditions are lower; the pore volumes are similarly smaller. In addition, the pore size distribution is wider (as seen in Figs. 6 and 7(f)).

The significant dependence of the specific surface area on the pore size can be seen by comparing the 100PSO and 10TEOS samples. Both samples have approximately the same pore volume (0.84 cm^3/g and 0.81 cm^3/g, respectively), but the specific surface areas vary significantly (1108.50 m^2/g versus 1953.94 m^2/g) due to the smaller pore size for the 10TEOS sample.

Table 3
Nitrogen adsorption results for the SiOC ceramics pyrolyzed in Ar and Ar + H_2O after the HF etching.

Sample	Specific surface area (m^2/g)		Micropore volume (cm^3/g)[a]		Total pore volume (m^3/g)		Average pore size (nm)	
	Ar	Ar + H_2O	Ar	Ar + H_2O	Ar	Ar + H_2O	Ar	Ar + H_2O
100PSO	880.1	1108.5	0.39	0.75	0.39	0.84	1.77	3.03
10PMPS	892.1	1356.9	0.40	0.82	0.40	0.93	1.79	2.74
10PDMS	886.9	952.9	0.41	0.54	0.41	0.59	1.85	2.48
10PHMS	952.6	1200.0	0.45	0.86	0.45	0.98	1.89	3.27
10TEOS	921.1	1953.9	0.43	0.81	0.44	0.81	1.91	1.66
10TMOS	653.4	804.2	0.35	0.45	0.37	0.48	2.27	2.39

[a] From t-plot analysis.

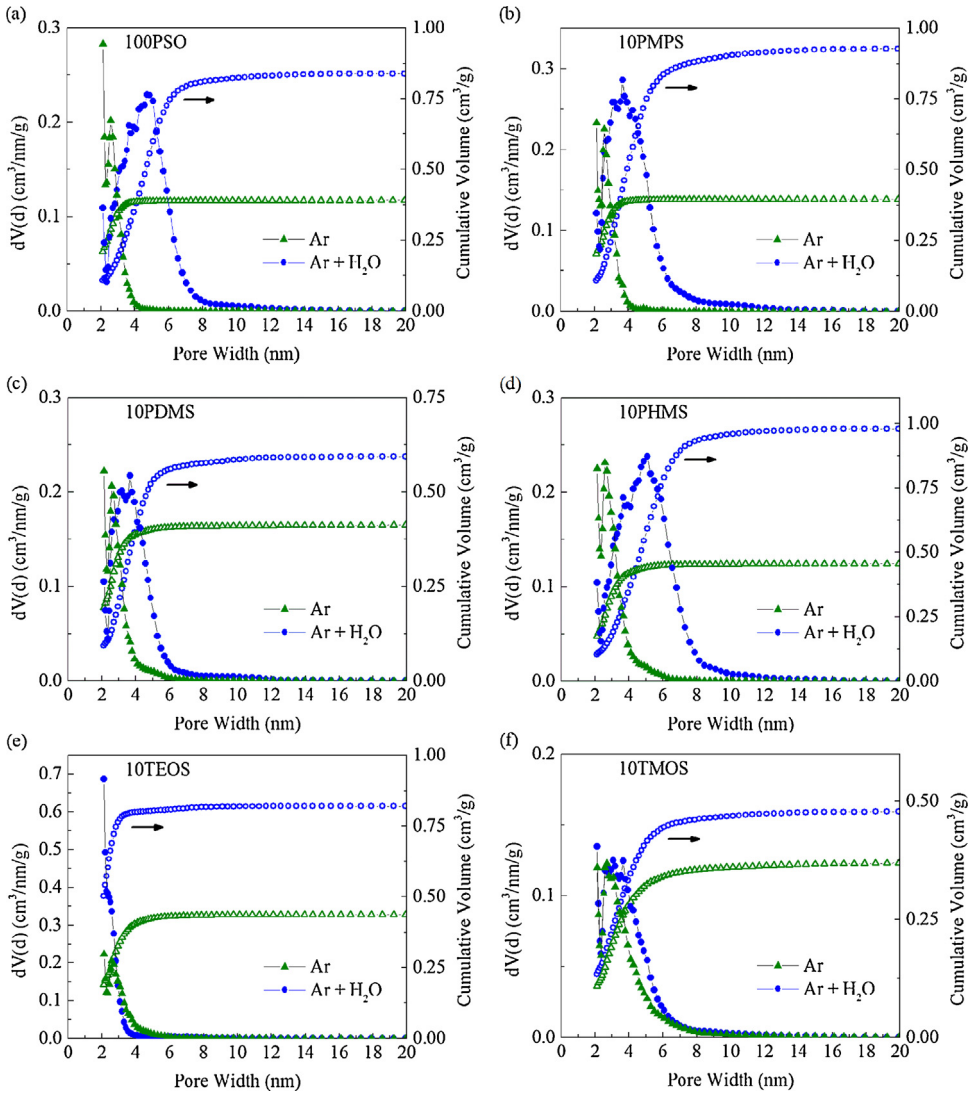

Fig. 7. Pore size distribution (filled symbols) and cumulative pore volume (unfilled symbols) for (a) 100PSO, (b) 10PMPS, (c) 10PDMS, (d) 10PHMS, (e) 10TEOS, and (f) 10TMOS.

For the samples pyrolyzed in Ar, the total pore volume ranges from 0.37 cm^3/g to 0.45 cm^3/g. The micropore volumes for the Ar samples are very close to the total pore volumes, indicating that all the samples are predominantly microporous (pore size <2 nm). For the samples with water vapor injection, the total pore volume increases for all the samples and ranges from 0.48 cm^3/g to 0.98 $cm^3/$. The micropore volumes for all of the samples with the Ar + H_2O atmosphere, except for 10TEOS, are slightly less than the total pore volume, indicating that mesopores (pore size 2–50 nm) are also present in the samples. The increase in total pore volume with the water vapor atmosphere can be attributed to the SiO_2 enrichment as discussed previously. The 10PHMS and 10PMPS samples have the largest pore volumes, 0.98 cm^3/g and 0.93 cm^3/g, respectively. However, the correlation of the pore volume increase after the HF etching with the additive type is a complex one because pore volume is a convoluted function of pore number density and pore size; it is also possible that some pore volume changes are not a simple result of SiO_2 removal if some C or SiOC is washed away during the HF etching due to their discontinuous distribution in the matrix [25].

Fig. 7 shows the pore size distributions and cumulative pore volumes for all the samples. For the additives that have the same Si/O ratio as the base PSO but different Si/C ratios (10PHMS, 10PDMS, 10PMPS), the pore size distributions for the Ar pyrolysis show that the polymers with higher carbon content (100PSO, 10PMPS) lead to narrower pore size distributions with smaller average pore sizes than the polymer with a lower carbon content (10PHMS). After the pyrolysis in Ar, the 10PHMS sample shows a slightly broader pore size distribution with pore widths up to approximately 6 nm while the 100PSO and 10PMPS samples have no pores larger than ~4 nm. This can be explained using the nanodomain model proposed by Saha et al. [40], and experimentally shown using small angle X-ray scattering [40] and nitrogen adsorption of etched SiOC [3,25]. According to this model, the SiO_2 clusters within the SiOC are separated by layers of turbostratic carbon. The carbon boundary layers effectively prevent nucleation and subsequently growth of the amorphous SiO_2 nanodomains by slowing diffusion [34]. Thus, the samples that are lower in carbon content (PHMS) produce larger SiO_2 domains, and larger pores after the HF etching. The effect of carbon preventing SiO_2 growth is further demonstrated from the results with water vapor pyrolysis: the 10PMPS sample again has a much narrower pore size distribution than the 10PHMS sample.

From the cumulative pore volume plots in Fig. 7, only 10TMOS and 10TEOS show an increase in pore volume at pores <2.1 nm from the Ar + H_2O pyrolysis compared to the Ar pyrolysis. In addition, the Ar + H_2O pyrolysis causes all the samples except for 10TEOS

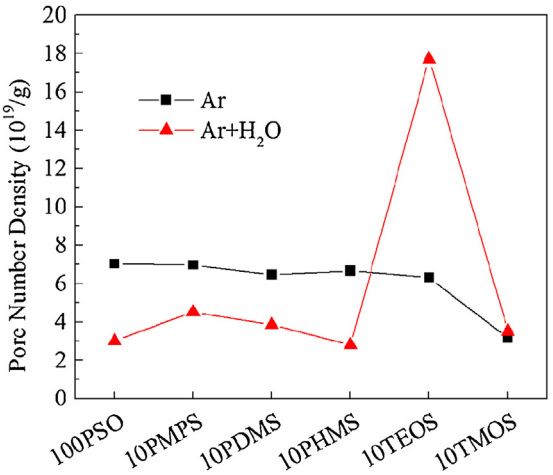

Fig. 8. Pore number density results calculated from Eq. (13) for the Ar and Ar + H_2O atmosphere pyrolyzed SiOC samples.

to have a larger average pore size and a wider pore size distribution, although the pore size distribution of the 10TMOS sample only slightly widens. This difference between the effects of the water vapor treatment on the 10TEOS and 10TMOS samples compared to the rest of the samples can be attributed to the reaction differences for these additives with water vapor. In addition to the reactions in Eqs. (3)–(8), the TEOS and TMOS additives themselves may also hydrolyze in the presence of water vapor:

$$Si{-}O{-}R + H_2O \rightarrow Si{-}OH + ROH \quad (12)$$

Where R is either CH_3 or C_2H_5. The Si—OH groups will then further condense into Si—O—Si following Eq. (9). This additional reaction for the 10TEOS and 10TMOS samples promotes further nucleation of SiO_2-rich regions within the samples after the Ar + H_2O pyrolysis at 700 °C, which leads to a higher number of SiO_2 domains after pyrolysis at 1400 °C.

The pore number density within the SiOC can be estimated using the pore volume and average pore size results. Assuming cylindrical pores, the pore density n is proportional to the pore volume divided by the product of the square of the average pore diameter d and the pore length. Further assuming that the pore length is proportional to the pore diameter, the pore number density is then given as:

$$n \propto \frac{V}{d^3} \quad (13)$$

Eq. (13) is plotted in Fig. 8 using the pore volume and average pore diameter values listed in Table 3. For the samples pyrolyzed in Ar, the pore number density is nearly constant for all the samples except for 10TMOS, which has approximately half the pore number density of the other samples and is consistent with our earlier conjecture that TMOS hydrolysis contributes partly to the SiOC matrix-based SiO_2 nucleation and growth. For the Ar + H_2O pyrolysis, the 100PSO, 10PMPS, 10PDMS, and 10PHMS samples all have approximately half of the pore number density of that from the Ar pyrolysis, and the 10TMOS sample shows a pore number density approximately equal to that from the Ar pyrolysis. In contrast, the 10TEOS sample after Ar + H_2O pyrolysis has a pore number density nearly three times higher than that for the Ar pyrolysis. This significant increase can be attributed to the hydrolysis of TEOS in the Ar + H_2O atmosphere according to Eq. (12). Interestingly, the

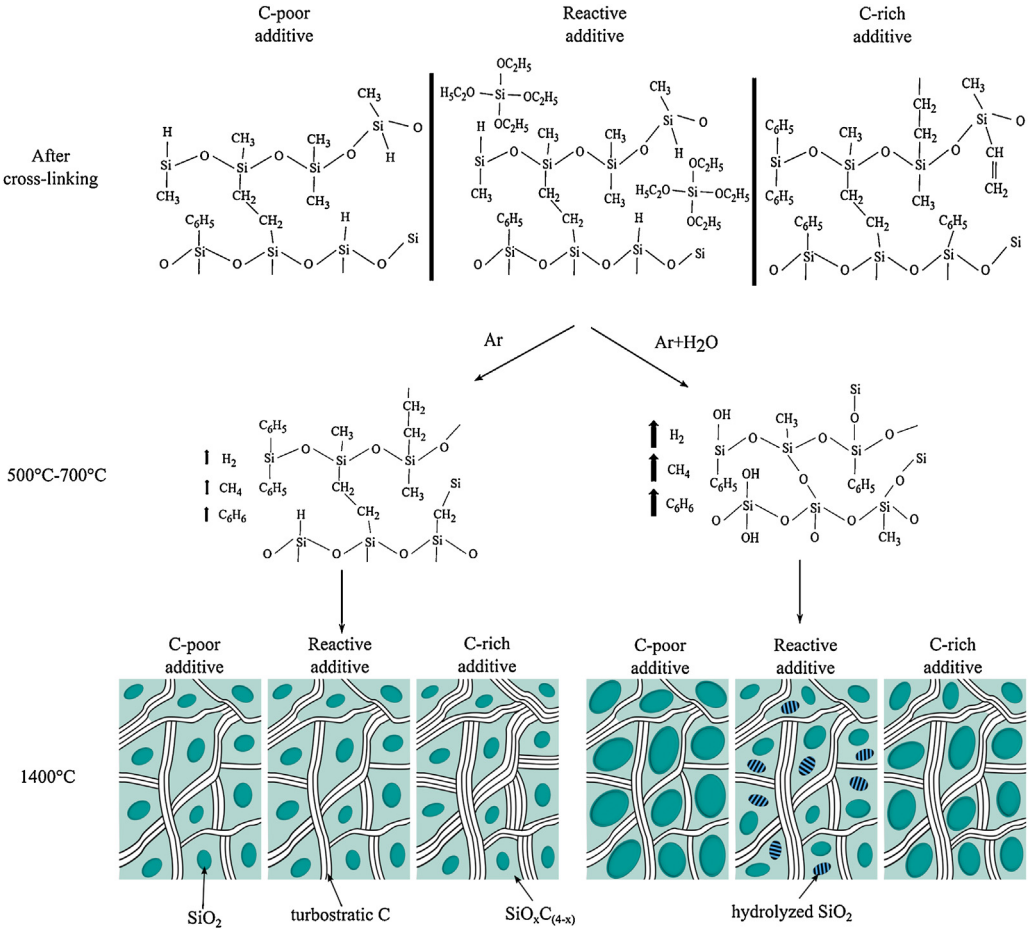

Fig. 9. Illustration showing the effect of additives and pyrolysis atmosphere on the microstructure of SiOC.

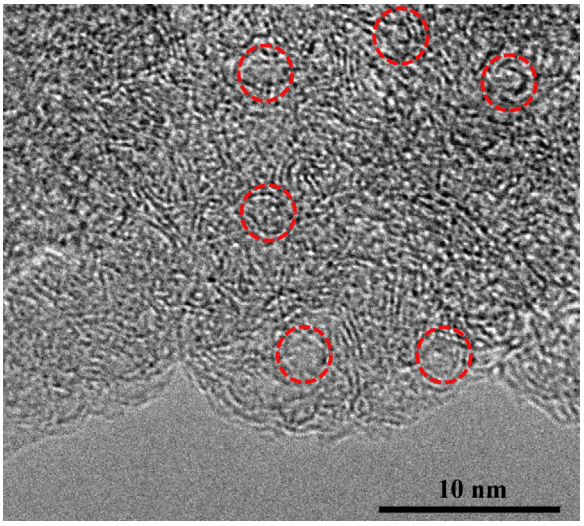

Fig. 10. TEM image of the 10TEOS Ar + H_2O sample after etching, with dashed circles indicating selected pores.

10TMOS sample does not show the same increase with the Ar + H_2O atmosphere although it should also hydrolyze according to Eq. (12).

3.4. Fundamental understanding

The effect of additives and pyrolysis atmosphere on the microstructural evolution of the SiOC is depicted in Fig. 9, taking into account the XRD, FT-IR, and nitrogen adsorption results. For PSO with different additives, pyrolysis in inert Ar produces very similar morphologies, with SiO_2 domains, amorphous SiOC surrounding SiO_2, and turbostratic carbon outside SiOC. The SiO_2 amount and size vary based on the additive used (as discussed in Section 3.3). Pyrolysis with water vapor injection, however, removes radical carbon species before they evolve into free carbon and are locked in the SiOC matrix. As a result, this reduces the turbostratic carbon layer thickness and converts more of the amorphous SiOC into SiO_2 rich domains [15]. For polymer precursors that are rich in carbon, the resulting ceramic is able to retain more of the free carbon and produce smaller sized SiO_2 domains compared to the carbon-poor samples. The addition of water-reactive species produces more SiO_2 nuclei with the water vapor pyrolysis, leading to a higher concentration of small SiO_2 domains after pyrolysis.

In the special case of the TEOS addition, TEOS itself can hydrolyze significantly and form independent SiO_2 clusters. As a result, the SiO_2 domains in the resulting SiOC matrix come from two sources: the SiOC matrix and the TEOS hydrolysis. Because of their small sizes (<2 nm), these SiO_2 nanodomains of different origins remain independent as depicted in Fig. 9 and lead to high specific surface areas after the HF etching. The pore morphology for the 10TEOS Ar + H_2O sample after the HF etching under TEM examination is shown in Fig. 10. Compared to the 100PSO sample, whose microstructure after the water vapor pyrolysis and HF etching is shown by Lu et al. [17], the 10TEOS sample contains more numerous, small, independent pores which supports the microstructure formation shown in Fig. 9.

Assuming that the turbostratic carbon content remains consistent for all the samples in the same pyrolysis atmosphere, the intensity ratios of SiO_2/C and SiC/C for the Ar and Ar + H_2O pyrolyzed samples are shown in Fig. 11. The selected peaks for deriving the ratios are 2θ values of 23°, 36°, and 44° for SiO_2, SiC, and C, respectively. As seen, for the Ar atmosphere, the SiO_2/C ratio is lower than the SiC/C ratio, meaning that the Si—O—Si bond formation is unfavorable. For different samples, the SiO_2/C and SiC/C

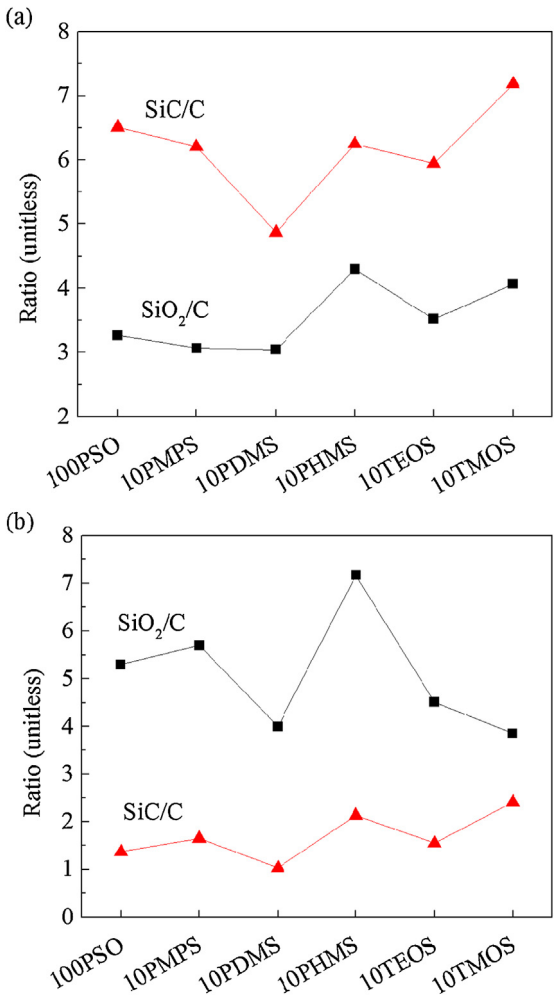

Fig. 11. SiO_2/C and SiC/C XRD relative intensity ratios for (a) Ar and (b) Ar + H_2O atmospheres.

ratios change consistently. Higher SiO_2/C ratios lead to higher SiC/C ratios and vice versa. This means that SiO_2 is easily consumed and SiC formation is directly dependent on the Si amount in the SiOC system. However, based on Eqs. (1)–(2), SiC formation is not at the expense of SiO_2. Otherwise, C content would significantly decrease. This means that in the evolving system, the phase separation of SiOC into SiO_2, SiC, and C (Eq. (1)) is more dominant than the carbothermal reaction in Eq. (2). Thus, the consumption of SiO_2 for the SiC formation is minimal. The generation of C from the SiOC phase separation also means that the C content increases without changing the SiO_2/C and SiC/C ratios.

For the Ar + H_2O atmosphere, the SiO_2/C ratio is much higher than the SiC/C ratio. For different samples, the SiO_2/C and SiC/C ratios also change consistently. This means that the Si for the SiO_2 and SiC formation is still from the phase separation of SiOC, which is not surprising considering the more dominant presence of SiOC (Fig. 3). However, due to the significant presence of SiO_2, the formation of SiC is suppressed and the SiC/C ratio is much lower than the SiO_2/C ratio.

A direct comparison of the SiO_2/SiC ratios in the Ar and Ar + H_2O samples are shown in Fig. 12(a). The SiO_2 intensity is 3–6 times of the SiC intensity for the Ar + H_2O sample while for the Ar sample the ratio is 0.5. The suppression of the SiC formation with the high amount of SiO_2 present in the Ar + H_2O atmosphere is clear, mainly because of the low amount of SiOC available for phase separation. The drastically smaller amount of SiO_2 content for the 10TMOS

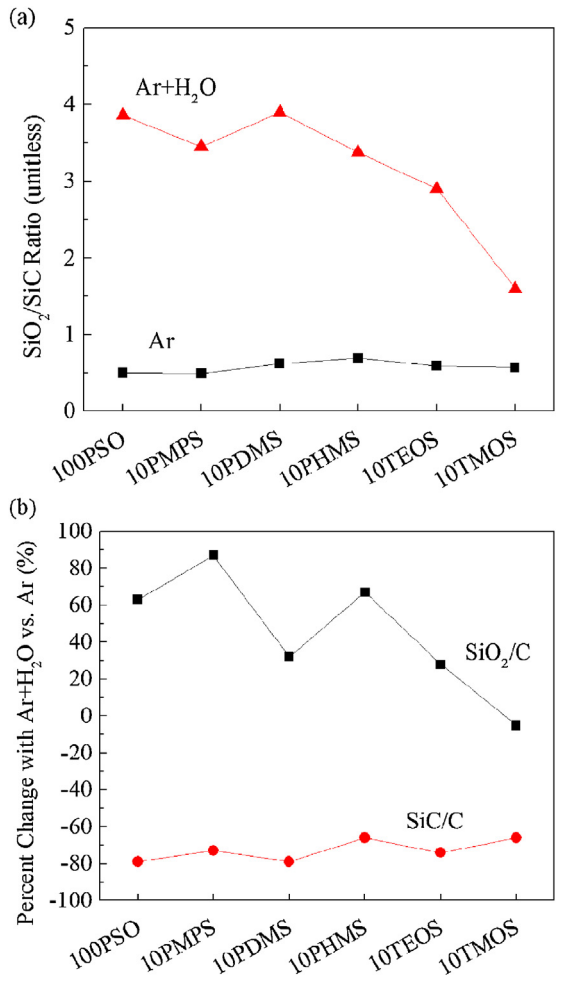

Fig. 12. (a) SiO_2/SiC XRD intensity ratios for Ar and Ar + H_2O pyrolysis, and (b) percent change of the SiO_2/C and SiC/C XRD ratios from the Ar + H_2O pyrolysis compared to the Ar pyrolysis.

sample is likely a result of the intimate mixing of the hydrolyzed Si—O bonds within the SiOC matrix. Thus, less SiO_2 is present even though the SiC formation is not hindered to any observable degree. Fig. 12(b) shows the percentage change of the SiO_2/C and SiC/C ratios with the Ar + H_2O pyrolysis compared to the Ar pyrolysis due to the SiO_2 formation increase and SiC formation decrease. In the Ar + H_2O atmosphere, PDMS has the least impact on the SiO_2/C ratio for the carbon-rich additives, PMPS has the highest impact, and PHMS gives a similar ratio as the pure PSO. For the TEOS and TMOS additives, the effect is lowest. For the 10TMOS sample, especially, the impact is negligible. This means that TMOS is highly mixed with the PSO precursor in the matrix. As a result, the SiO_2/C ratio only increases to a negligible degree. The percent change of the SiC/C ratio with the Ar + H_2O pyrolysis in Fig. 12(b) is relatively constant for all of the samples. This confirms that the SiO_2, SiC, and C formation occurs almost solely from the phase separation of SiOC following Eq. (1) because the phase separation of SiOC creates equal amounts of SiC and C. If carbothermal reduction of SiO_2 was the cause of the SiO_2/C ratio differences between additives seen in Fig. 12(b), then the SiC/C ratio would show a similar change rather than being nearly the same for all the samples.

4. Conclusions

Highly porous SiOC ceramics are produced by pyrolysis in Ar and Ar + H_2O environments. The presence of water vapor during pyrolysis facilitates the formation of Si—O bonds, leading to significantly more SiO_2 after pyrolysis to 1400 °C. SiO_2 formation in Ar creates an average pore size ranging from 1.77 nm to 2.27 nm. The specific surface area and pore volume values range from 653.41 m^2/g to 952.64 m^2/g and 0.37 cm^3/g to 0.45 cm^3/g, respectively. With water vapor pyrolysis, there is a significant difference in specific surface areas for different additives, ranging from 804.24 m^2/g for the 10TMOS sample to 1953.94 m^2/g for the 10TEOS sample; the average pore sizes remain in the <4 nm range. The effects of the additives and atmosphere on the SiOC microstructural evolution are explained and the SiO_2 vs. SiC formation mechanisms are presented. The ability to drastically increase the specific surface area of the SiOC ceramics through additives and pyrolysis atmosphere presents a new and promising processing route for creating highly porous ceramics.

Acknowledgements

We acknowledge the financial support from National Science Foundation under grant number CMMI-1634325.

References

[1] P. Colombo, G. Mera, R. Riedel, G.D. Soraru, Polymer-derived ceramics: 40 years of research and innovation in advanced ceramics, J. Am. Ceram. Soc. 93 (2010) 1805–1837.
[2] K. Lu, D. Erb, M. Liu, Thermal stability and electrical conductivity of carbon-enriched silicon oxycarbide, J. Mater. Chem. C 4 (2016) 1829–1837.
[3] K. Lu, D. Erb, M.Y. Liu, Phase transformation oxidation stability, and electrical conductivity of TiO_2-polysiloxane derived ceramics, J. Mater. Sci. 51 (2016) 10166–10177.
[4] Y. Juttke, H. Richter, I. Voigt, R.M. Prasad, M.S. Bazarjani, A. Gurlo, R. Riedel, Polymer derived ceramic membranes for gas separation, Chem. Eng. Trans. 32 (2013) 1891–1896.
[5] J.K. Li, K. Lu, T.S. Lin, F.Y. Shen, Preparation of micro-/mesoporous SiOC bulk ceramics, J. Am. Ceram. Soc. 98 (2015) 1753–1761.
[6] Y. Blum, G.D. Soraru, A.P. Ramaswamy, D. Hui, S.M. Carturan, Controlled mesoporosity in SiOC via chemically bonded polymeric spacers, J. Am. Ceram. Soc. 96 (2013) 2785–2792.
[7] P. Colombo, Engineering porosity in polymer-derived ceramics, J. Eur. Ceram. Soc. 28 (2008) 1389–1395.
[8] K. Lu, Porous and high surface area silicon oxycarbide-based materials-A review, Mat. Sci. Eng. 97 (2015) 23–49.
[9] J.L. Wan, M.J. Gasch, A.K. Mukherjee, In situ densification behavior in the pyrolysis consolidation of amorphous Si-N-C bulk ceramics from polymer precursors, J. Am. Ceram. Soc. 84 (2001) 2165–2169.
[10] H. Brequel, J. Parmentier, G.D. Soraru, L. Schiffini, S. Enzo, Study of the phase separation in amorphous silicon oxycarbide glasses under heat treatment, Nanostruct. Mater. 11 (1999) 721–731.
[11] A. Saha, R. Raj, Crystallization maps for SiCO amorphous ceramics, J. Am. Ceram. Soc. 90 (2007) 578–583.
[12] L. Biasetto, R. Pena-Alonso, G.D. Soraru, P. Colombo, Etching of SiOC ceramic foams, Adv. Appl. Ceram. 107 (2008) 106–110.
[13] Y.D. Blum, D.B. MacQueen, H.-J. Kleebe, Synthesis and characterization of carbon-enriched silicon oxycarbides, J. Eur. Ceram. Soc. 25 (2005) 143–149.
[14] C. Turquat, H.J. Kleebe, G. Gregori, S. Walter, G.D. Soraru, Transmission electron microscopy and electron energy-loss spectroscopy study of nonstoichiometric silicon-carbon-oxygen glasses, J. Am. Ceram. Soc. 84 (2001) 2189–2196.
[15] T. Liang, Y.-L. Li, D. Su, H.-B. Du, Silicon oxycarbide ceramics with reduced carbon by pyrolysis of polysiloxanes in water vapor, J. Eur. Ceram. Soc. 30 (2010) 2677–2682.
[16] M. Narisawa, K. Terauds, R. Raj, Y. Kawamoto, T. Matsui, A. Iwase, Oxidation process of white Si-O-C(-H) ceramics with various hydrogen contents, Scripta Mater. 69 (2013) 602–605.
[17] K. Lu, J. Li, Fundamental understanding of water vapor effect on SiOC evolution during pyrolysis, J. Eur. Ceram. Soc. 36 (2016) 411–422.
[18] J.K. Li, K. Lu, Highly Porous SiOC bulk ceramics with water vapor assisted pyrolysis, J. Am. Ceram. Soc. 98 (2015) 2357–2365.
[19] K. Tsougeni, A. Tserepi, E. Gogolides, Photosensitive poly(dimethylsiloxane) materials for microfluidic applications, Microelectron. Eng. 84 (2007) 1104–1108.
[20] N. Janakiraman, F. Aldinger, Fabrication and characterization of fully dense Si-C-N ceramics from a poly (ureamethylvinyl) silazane precursor, J. Eur. Ceram. Soc. 29 (2009) 163–173.
[21] S. Martinez-Crespiera, E. Ionescu, H.J. Kleebe, R. Riedel, Pressureless synthesis of fully dense and crack-free SiOC bulk ceramics via photo-crosslinking and pyrolysis of a polysiloxane, J. Eur. Ceram. Soc. 31 (2011) 913–919.

[22] J.T. Sun, Y.D. Huang, H.L. Cao, G.F. Gong, Effects of ambient-temperature curing agents on the thermal stability of poly(methylphenylsiloxane), Polym. Degrad. Stab. 85 (2004) 725–731.
[23] P.I. Ravikovitch, A.V. Neimark, Characterization of nanoporous materials from adsorption and desorption isotherms, Colloids Surf. A 187 (2001) 11–21.
[24] J. Rouquerol, P. Llewellyn, F. Rouquerol, Is the BET equation applicable to microporous adsorbents? Stud. Surf. Sci. Catal. 160 (2006) 49–56.
[25] R. Peña-Alonso, G.D. Sorarù, R. Raj, Preparation of ultrathin-walled carbon-based nanoporous structures by etching pseudo-amorphous silicon oxycarbide ceramics, J. Am. Ceram. Soc. 89 (2006) 2473–2480.
[26] A.K. Singh, C.G. Pantano, The role of Si-H functionality in oxycarbide glass synthesis, Mater. Res. Soc. Symp. P. 271 (1992) 795–800.
[27] M. Halim, C. Hudaya, A.Y. Kim, J.K. Lee, Phenyl-rich silicone oil as a precursor for SiOC anode materials for long-cycle and high-rate lithium ion batteries, J. Mater. Chem. A 4 (2016) 2651–2656.
[28] G.W. Liu, J. Kaspar, L.M. Reinold, M. Graczyk-Zajac, R. Riedel, Electrochemical performance of DVB-modified SiOC and SiCN polymer-derived negative electrodes for lithium-ion batteries, Electrochim. Acta 106 (2013) 101–108.
[29] A. Nyczyk-Malinowska, M. Wojcik-Bania, T. Gumula, M. Hasik, M. Cypryk, Z. Olejniczak, New precursors to SiCO ceramics derived from linear poly(vinylsiloxanes) of regular chain composition, J. Eur. Ceram. Soc. 34 (2014) 889–902.
[30] D.R. Anderson, Infrared, raman, and ultraviolet spectroscopy, in: A.L. Smith (Ed.), Analysis of Silicones, Robert E. Krieger Publishing Company, Inc., Malabar, FL, 1983, pp. 257–279.
[31] A.M. Wilson, G. Zank, K. Eguchi, W. Xing, B. Yates, J.R. Dahn, Pore creation in silicon oxycarbides by rinsing in dilute hydrofluoric acid, Chem. Mater. 9 (1997) 2139–2144.
[32] R. Pena-Alonso, G. Mariotto, C. Gervais, F. Babonneau, G.D. Soraru, New insights on the high-temperature nanostructure evolution of SiOC and B-doped SiBOC polymer-derived glasses, Chem. Mater. 19 (2007) 5694–5702.
[33] Z.Q. Li, C.J. Lu, Z.P. Xia, Y. Zhou, Z. Luo, X-ray diffraction patterns of graphite and turbostratic carbon, Carbon 45 (2007) 1686–1695.
[34] H.J. Kleebe, C. Turquat, G.D. Soraru, Phase separation in an SiCO class studied by transmission electron microscopy and electron energy-loss spectroscopy, J. Am. Ceram. Soc. 84 (2001) 1073–1080.
[35] G. Tobias, L.D. Shao, C.G. Salzmann, Y. Huh, M.L.H. Green, Purification and opening of carbon nanotubes using steam, J. Phys. Chem. B 110 (2006) 22318–22322.
[36] G.D. Soraru, R. Pena-Alonso, M. Leoni, C-rich micro/mesoporous Si(B)OC: In situ diffraction analysis of the HF etching process, Micropor. Mesopor. Mater. 172 (2013) 125–130.
[37] G.D. Soraru, S. Modena, E. Guadagnino, P. Colombo, J. Egan, C. Pantano, Chemical durability of silicon oxycarbide glasses, J. Am. Ceram. Soc. 85 (2002) 1529–1536.
[38] X.Y. Yuan, H.L. Jin, X.B. Yan, L.F. Cheng, L.T. Hu, Q.J. Xue, Synthesis of ordered mesoporous silicon oxycarbide monoliths via preceramic polymer nanocasting, Micropor. Mesopor. Mater. 147 (2012) 252–258.
[39] K.S.W. Sing, Reporting physisorption data for gas solid systems – with special reference to the determination of surface-area and porosity, Pure Appl. Chem. 54 (1982) 2201–2218.
[40] A. Saha, R. Raj, D.L. Williamson, A model for the nanodomains in polymer-derived SiCO, J. Am. Ceram. Soc. 89 (2006) 2188–2195.